



The SWELLS survey – III. Disfavouring ‘heavy’ initial mass functions for spiral lens galaxies

Brendon J. Brewer,¹★ Aaron A. Dutton,^{1,2,3}† Tommaso Treu,¹‡ Matthew W. Auger,^{1,4}
 Philip J. Marshall,^{5,6} Matteo Barnabè,⁵ Adam S. Bolton,⁷ David C. Koo³ and
 Léon V. E. Koopmans⁸

¹Department of Physics, University of California, Santa Barbara, CA 93106, USA

²Department of Physics and Astronomy, University of Victoria, Victoria, BC V8P 5C2, Canada

³UCO/Lick Observatory, Department of Astronomy and Astrophysics, University of California, Santa Cruz, CA 95064, USA

⁴Institute of Astronomy, University of Cambridge, Madingley Road, Cambridge CB3 0HA

⁵Kavli Institute for Particle Astrophysics and Cosmology, Stanford University, 452 Lomita Mall, Stanford, CA 94035, USA

⁶Department of Physics, University of Oxford, Keble Road, Oxford OX1 3RH

⁷Department of Physics and Astronomy, University of Utah, Salt Lake City, UT 84112, USA

⁸Kapteyn Astronomical Institute, University of Groningen, PO Box 800, 9700 AV Groningen, the Netherlands

Accepted 2012 March 2. Received 2012 March 1; in original form 2012 January 8

ABSTRACT

We present gravitational lens models for 20 strong gravitational lens systems observed as part of the Sloan WFC Edge-on Late-type Lens Survey (SWELLS) project. 15 of the lenses are taken from Paper I, while five are newly discovered systems. The systems are galaxy–galaxy lenses where the foreground deflector has an inclined disc, with a wide range of morphological types, from late-type spiral to lenticular. For each system, we compare the total mass inside the critical curve inferred from gravitational lens modelling to the stellar mass inferred from stellar population synthesis (SPS) models, computing the stellar mass fraction $f^* \equiv M_{\text{SPS}}/M_{\text{lens}}$. We find that, for the lower mass SWELLS systems, adoption of a Salpeter stellar initial mass function (IMF) leads to estimates of f^* that exceed 1. This is unphysical and provides strong evidence against the Salpeter IMF being valid for these systems. Taking the lower mass end of the SWELLS sample ($\sigma_{\text{SIE}} < 230 \text{ km s}^{-1}$), we find that the IMF is lighter (in terms of stellar mass-to-light ratio) than Salpeter with 98 per cent probability, and consistent with the Chabrier IMF and IMFs between the two. This result is consistent with previous studies of spiral galaxies based on independent techniques. In combination with recent studies of massive early-type galaxies that have favoured a heavier Salpeter-like IMF, this result strengthens the evidence against a universal stellar IMF.

Key words: gravitational lensing: strong – stars: luminosity function, mass function – galaxies: fundamental parameters – galaxies: spiral.

1 INTRODUCTION

The stellar initial mass function (IMF) is a fundamental property of a simple stellar population and plays a key role in many astrophysical problems. For instance, the determination of galaxy stellar masses and star formation rates are uncertain at the factor of ~ 2 level due to uncertainty in the IMF (e.g. Panter et al. 2007; Conroy, Gunn & White 2009).

Observations of the solar neighbourhood favour an IMF with a power-law slope at high masses (Salpeter 1955) and a turnover at low masses (Kroupa 2001; Chabrier 2003). While other spiral galaxies have IMFs consistent with that of the Milky Way (Bell & de Jong 2001; Bershady et al. 2011; Dutton et al. 2011a,b; Suyu et al. 2011), there is increasing evidence from a variety of observations that the IMF is non-universal. Specifically, massive early-type galaxies at low redshifts require IMFs that are heavier than in the Milky Way (e.g. Auger et al. 2010b; Sonnenfeld et al. 2011; Spinelli et al. 2011), and possibly heavier than Salpeter in the most massive ellipticals (van Dokkum & Conroy 2010). Other lensing and dynamical studies of early-type galaxies also suggest that the IMF may be heavy (Treu et al. 2010; Thomas et al. 2011) although these

★E-mail: brewer@physics.ucsb.edu;

†CITA National Fellow.

‡Packard Research Fellow.

observations may also be explained by a trend in the properties of the dark matter haloes. Recently, variations in the IMF of early-type galaxies have also been reported by Cappellari et al. (2012) and Dutton, Mendel & Simard (2012).

One of the simplest ways of constraining the galaxy-averaged IMF is through comparing total masses (within some aperture), as derived by kinematics and/or strong gravitational lensing and referred to as gravitational masses henceforth, with stellar masses derived from stellar population synthesis (SPS) models (Cappellari et al. 2006; Ferreras et al. 2010; Thomas et al. 2011). While this method typically only provides strong upper limits to the stellar mass due to the unknown dark matter fraction, as well as the unknown mass in gas, dust, etc., the upper limits are robust.

Dark matter fractions in galaxies are expected to increase with radius, so the strongest constraints on the IMF (from total mass measurements) come from measuring mass-to-light ratios at small galactic radii. However, at small radii, kinematics are harder to interpret, as there is usually a mix of rotation and dispersion. This is where strong gravitational lensing is particularly useful and unique, because it measures projected mass independent of the dynamical state of the deflector.

Assuming a universal IMF, the dark matter fractions within the effective radius of early-type galaxies decrease with decreasing mass (down to a stellar mass of $\simeq 10^{10} M_{\odot}$) (e.g. Padmanabhan et al. 2004; Gallazzi et al. 2006; Auger et al. 2010a; Barnabè et al. 2011; Dutton et al. 2011a). Thus lower mass elliptical galaxies are expected to place stronger constraints on the IMF than higher mass elliptical galaxies (although high-mass systems can place strong constraints as well through dynamics; e.g. Spinelli et al. 2011). If the bulges of spiral galaxies follow the same scaling relations as elliptical galaxies, then we would expect that bulges of mass $\simeq 10^{10} M_{\odot}$ – where the dark matter fraction is minimized – would provide the strongest constraints on the IMF if the IMF is universal (e.g. Bastian, Covey & Meyer 2010; Kroupa et al. 2011). Conversely, if the IMF is not universal, measuring it as a function of galaxy mass, morphology and environment should help understand the physical mechanisms that determine it.

Measuring the absolute normalization of stellar IMF as a function of galaxy type and mass is one of the main goals of the Sloan WFC Edge-on Late-type Lens Survey (SWELLS; Treu et al. 2011, hereafter Paper I; Dutton et al. 2011b, hereafter Paper II).

In this paper, we present *Hubble Space Telescope* (*HST*) multi-colour imaging of the complete SWELLS sample, including new data from cycle 18 observations, and use strong lensing models to constrain the stellar IMF of spiral galaxies. In particular, we use precision measurements of the total mass within the critical curve and therefore place an upper limit on the amount of stellar mass. We combine this inferences with stellar masses derived from SPS models to obtain strong upper limits on the normalization of the stellar IMF.

The galaxies in the SWELLS sample have total stellar masses (assuming a Chabrier IMF) of $M_* \simeq 4-30 \times 10^{10} M_{\odot}$ and bulge masses of $\simeq 2-10 \times 10^{10} M_{\odot}$ (Paper I). In order to explore the variation of the IMF with stellar mass, we combine our sample with the more massive elliptical galaxy lenses from the Sloan Lens ACS (Advanced Camera for Surveys) Survey (SLACS) (Auger et al. 2009) with $M_* \simeq 10-50 \times 10^{10} M_{\odot}$.

Throughout this paper, we assume a flat Λ cold dark matter (Λ CDM) cosmology with present-day matter density, $\Omega_m = 0.3$, and Hubble parameter, $H_0 = 70 \text{ km s}^{-1} \text{ Mpc}^{-1}$.

2 THE DATA

In this section we briefly summarize the sample selection procedure (Section 2.1; more details can be found in Paper I) and then present the new cycle 18 *HST* observations in Section 2.2.

2.1 Sample selection

The sample of spiral lens galaxy candidates was selected from the Sloan Digital Sky Survey (SDSS) data base as discussed in Paper I. Briefly, the spectroscopic data base was searched for composite spectra, consisting of foreground spectrum superimposed with multiple emission lines at a higher redshifts, following the procedures developed for the SLACS (Bolton et al. 2006, 2008, hereafter B06 and B08, respectively) and the BOSS (Baryon Oscillation Spectroscopic Survey) Emission-Line Lensing Survey (BELLS; Brownstein et al. 2012) surveys. In addition, however, in order to identify inclined late-type galaxies suitable for rotation curve measurements, the deflector galaxies were selected to have axis ratios $q = b/a \gtrsim 0.6$ with a preference for galaxies with edge-on discs and emission lines indicating star formation. A priori lensing probabilities were estimated based on the SDSS stellar velocity dispersion and stellar Einstein radius (Paper I).

2.2 HST observations and surface photometry

The highest probability lens candidates were followed up with *HST* in supplemental cycle 16s programme (GO-11978; PI: Treu) and are presented in Paper I. In addition, during the same programme, multiband imaging was obtained for disc lens galaxies identified as part of the SLACS survey (GOs 10174, 10494, 10798, 11202, PI: Koopmans; GOs 10587, 10886, PI: Bolton). Lower probability systems were included in a cycle 18 programme (GO-12292; PI: Treu), aiming to extend the sample to later type spirals, and are presented here for the first time. Two candidates confirmed from the ground with adaptive optics (AO; Paper I) were also included in the cycle 18 programme to collect optical multiband photometry. 21 candidates were observed in cycle 18. 18 of those were observed with the refurbished Advanced Camera for Surveys (ACS) for one orbit each, split equally between filters *F435W* and *F814W*. Two dithered exposures were obtained for each filter to aid in cosmic ray and defect removal and to help improve the sampling of the point spread function (PSF). Four candidates, including one observed with ACS were observed with the infrared channel of the Wide Field Camera 3 for a full orbit through filter *F160W*. Each orbit was split into four dithered exposures to aid in cosmic ray and defect removal and help improve the sampling of the PSF. The *HST* images were reduced using standard multidrizzle techniques. As expected, the fraction of grade ‘A’ and ‘B’ lenses was lower for cycle 18 than for previous cycles, 6/21 and 10/21, respectively; images for these 21 systems are displayed in Fig. 1.

In total, after *HST* imaging, the SWELLS sample consists of 20 secure lenses (grade ‘A’), six probable lenses (grade ‘B’) and 12 possible lenses (grade ‘C’). Grade ‘A’ lenses are defined as having unambiguous multiple images successfully reproduced by a reasonably simple lens model. Grade ‘B’ lenses are defined as having evidence for strong lensing, even though the quality of the data is not sufficient to identify unambiguously multiple images and/or construct a lens model. This definition is quite conservative and we expect that with deeper data or narrow-band imaging data to facilitate removal of the foreground deflector light, most ‘B’ grade systems would be confirmed as lenses. Grade ‘C’ are possible

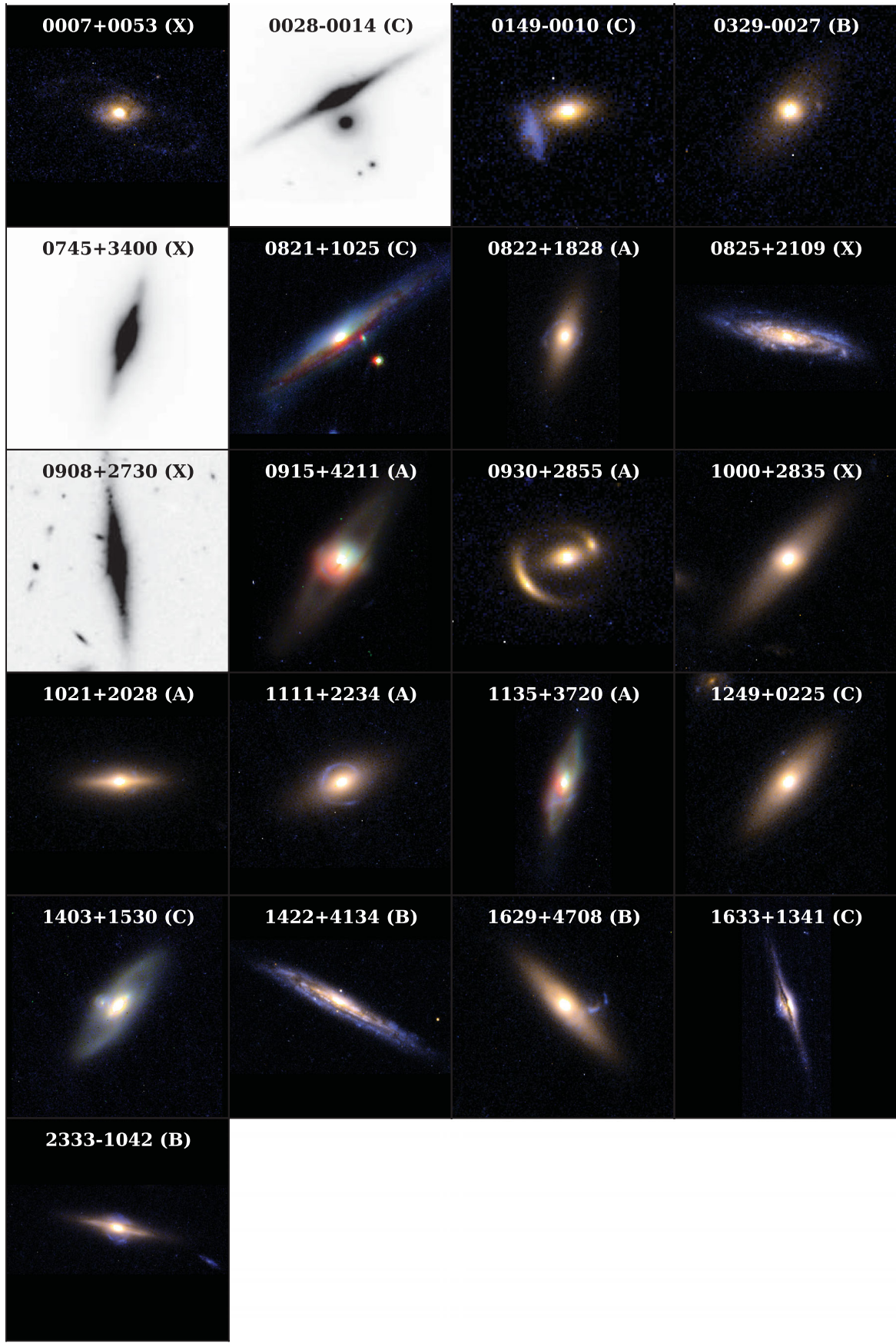


Figure 1. Images of the 21 candidate lens systems observed with the *HST* during cycle 18; the grade of each system is provided in parentheses next to the name.

lenses where we expect that even with significantly better data only a minority of the systems would be confirmed as lenses. A colour montage of the 20 grade ‘A’ lenses from SWELLS is shown in Fig. 2.

For this paper we focus our analysis on the grade ‘A’ lenses, plus one grade ‘B’ lens (J1422+4134), for which we were able to obtain a plausible lens model. However, in the light of the uncertain identification of this one system, we will use only the grade ‘A’ lenses for our inference on the stellar IMF. We also excluded one grade ‘A’ lens, J1037+3517, since the morphology of the lens is complex (involving a merger) and the modelling approach of this paper was unlikely to be successful for this system. A summary of the basic properties of the SWELLS lenses together with the inferred parameters of the gravitational lens models is given in Table 1. A summary of the basic properties of the SWELLS *HST* cycle 18 targets is given in Table 2.

Multiband surface photometry was derived as described in Paper I, by fitting two-component (bulge+disc) models using SPASMOID (Bennert et al. 2011). The model consists of an $n = 4$ Sérsic profile (i.e. a de Vaucouleurs profile; de Vaucouleurs 1948; Sérsic 1968) for the bulge and an $n = 1$ exponential disc component. Estimates of the model parameters, including stellar masses and mass-to-light ratios, are given in Tables 3–5.

3 GRAVITATIONAL LENS MODELS

In this section we describe the procedure used to obtain gravitational lens models for each system. We consider relatively simple mass models for the deflector, described as a singular isothermal ellipsoid (SIE) plus external shear (Kormann, Schneider & Bartelmann 1994). This simple model is known to provide a good description of (at least early type) galaxy-scale gravitational lenses (Barnabè et al. 2009; Koopmans et al. 2009; Treu 2010), and should provide sufficiently robust estimates of the physical quantities relevant for this present analysis, i.e. the mass enclosed within the critical curve and the position angle and the ellipticity of the mass distribution. The flat rotation curves of spiral galaxies (van Albada & Sancisi 1986) suggest that this model is appropriate for spiral lenses, at least to first order.

The modelling of the SWELLS lenses is complicated compared to typical gravitational lens modelling for several reasons. The first challenge is the disentanglement of the light of the source and that of the deflector. Our strategy to address this challenge is discussed in Section 3.1. An additional challenge is the proper estimation of model parameter uncertainties. This is discussed in Section 3.2 where we present our mass models and inference strategy. Finally, in Section 3.3 we discuss each individual system listing any additional complexities.

3.1 Disentangling the source and deflector light

The first step is the selection of the band which contains the highest fidelity image of the lensed features and will therefore be used to produce the lens model. In most cases this is the bluest image available, as the lensed features tend to be brightest at the blue end of the spectrum. In the cases where the lens galaxy contains significant amounts of dust, a redder band was selected to minimize complications from the dust.

Most significantly, the small Einstein radii of the lenses cause the lensed features to lie in regions where the surface brightness of the lens galaxy is non-negligible. This makes lens galaxy subtraction non-trivial. In principle, we should fit the light profile of the

lens galaxy simultaneously with any lensing parameters and source surface brightness profile parameters. We have attempted this, but found that it was too computationally intensive to be practical.

In addition, the light profiles of the lens galaxies cannot be described adequately by simple models such as the Sérsic profile (Sérsic 1968) due to the presence of dust lanes, star-forming regions and other complexities. Attempting to use such a profile would result in lens galaxy subtractions with significant residuals that would interfere with the modelling of the lensed features.

3.1.1 Rotation subtraction for masking

To proceed with the lens galaxy subtractions, we adopted the following procedure. First, for exploratory purposes, we take advantage of the near symmetry of the lens galaxy: by subtracting the image from a 180° rotated version of itself, the lensed features, often asymmetric, are revealed (see Fig. 3). The centre point around which the rotation takes place can be left as a free parameter, and optimized to find the centre of rotation which makes the rotated image best match the original image.

These rotation-subtracted images enable us to get an initial estimate for the position and morphology of the lensed features, particularly the identification of any faint counter-images. However, these images cannot be used as data for modelling because they contain both positive and negative reproductions of the arc.

In practice, we used the rotation-subtracted images to inform the placement of a masked region, covering the lensed features. With these features masked out, we fit a complex many-parameter model for the surface brightness profile of the lens galaxy, and subtract that model from the data, giving the final data for lens modelling.

3.1.2 Multi-Gaussian subtraction

With the mask in place, we fit the remaining pixels using the code of Brewer et al. (2011a), with all Sérsic indices set to $n = 1/2$ —i.e. we fit the lens galaxy with up to 10 elliptical Gaussian components (this is similar to the multi-Gaussian expansion method of Cappellari 2002). For the more complex galaxies with star-forming rings, we allow negative Gaussians to be included as well. The star-forming ring can be modelled as a smooth Gaussian-like profile with negative Gaussians suppressing interior surface brightness, resulting in a ring profile. We use the multi-Gaussian model to subtract the lens galaxy from the image, resulting in an image of the lensed features only. These lens-subtracted images are shown in the second column of Fig. 4.

3.2 Gravitational lens model

We fit SIE lens models with external shear to the lensed features of each system. The source plane position (x_s, y_s) and the image plane position (x, y) of a ray are related by

$$\begin{aligned} x_s &= x - \alpha_x(x, y), \\ y_s &= y - \alpha_y(x, y), \end{aligned} \quad (1)$$

where the deflection angles $\alpha_{x,y}$ are given by Keeton & Kochanek (1998). Defining $\psi = \sqrt{q^2 x^2 + y^2}$, where q is the axis ratio/flattening of the projected mass profile, the deflection angle formulae for the SIE component (i.e. before adding the external shear) are the following:

$$\alpha_x(x, y) = \frac{b\sqrt{q}}{\sqrt{1-q^2}} \tan^{-1} \left[\frac{x\sqrt{1-q^2}}{\psi} \right], \quad (2)$$

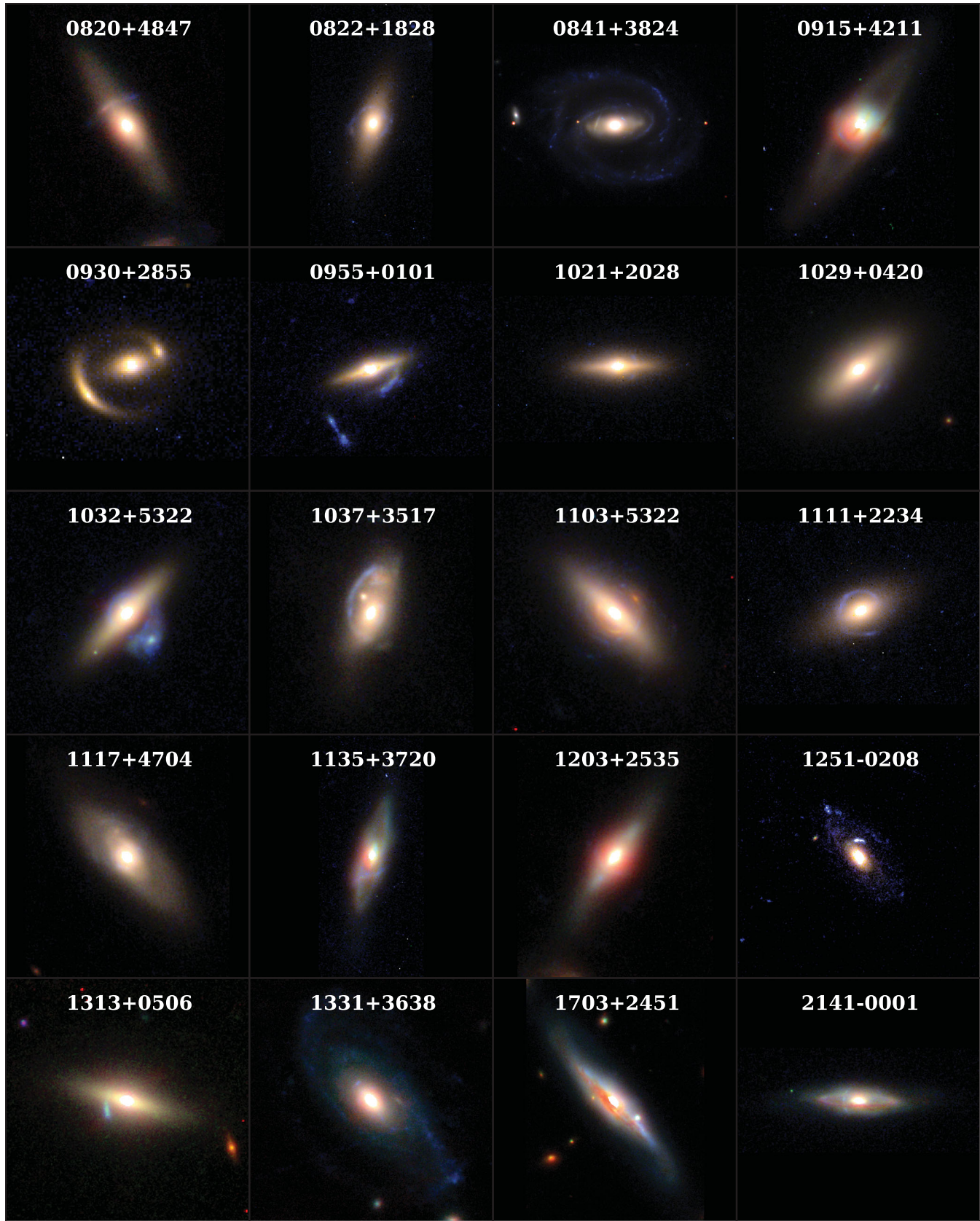


Figure 2. Images of the 20 grade ‘A’ lens systems that comprise the SWELLS sample.

Table 1. Summary of basic properties of modelled grade ‘A’ lenses (plus the modelled grade ‘B’ lens J1422+4134) from the SWELLS sample of spiral lens galaxies. Column 1 lists the lens ID; columns 2 and 3 the coordinates (J2000 in degrees); columns 4 and 5 give deflector and source redshifts; column 6 the Einstein radius of the lens model; column 7 the velocity dispersion of the SIE plus external shear (SIE+ γ) lens model; column 8 the axis ratio of the lens model; column 9 the projected mass within the critical curve of the SIE lens model; columns 10 and 11 the ratio between the stellar mass and lensing mass within the critical curve, assuming Chabrier and Salpeter IMF, respectively; column 12 is the reference for the lens discovery (1 = B06, 2 = B08, 3 = Paper I, 4 = this paper); column 13 is the band used for the lens modelling.

ID (1)	RA (2)	Dec. (3)	z_d (4)	z_s (5)	b (arcsec) (6)	σ_{SIE} (km s $^{-1}$) (7)	q (8)	M_{lens} ($10^{10} M_{\odot}$) (9)	f_{Chab}^* (10)	f_{Salp}^* (11)	Ref (12)	Band (13)
J0820+4847	125.05363	48.79364	0.131	0.634	0.82 ± 0.09	191.9 ± 10.7	0.19 ± 0.09	5.21 ± 1.15	0.70 ± 0.17	1.18 ± 0.28	3	F450W
J0822+1828	125.614474	18.482175	0.1153	0.8710	0.83 ± 0.03	185.1 ± 4.0	0.75 ± 0.08	4.36 ± 0.28	0.54 ± 0.17	1.03 ± 0.39	4	F435W
J0841+3824	130.37004	38.40381	0.116	0.657	1.46 ± 0.05	251.2 ± 4.4	0.70 ± 0.08	14.1 ± 0.99	0.51 ± 0.11	0.92 ± 0.18	2	F814W
J0915+4211	138.81787	42.19800	0.078	0.790	0.98 ± 0.02	195.7 ± 2.2	0.64 ± 0.08	4.03 ± 0.18	0.81 ± 0.18	1.44 ± 0.30	3	K p
J0930+2855	142.572560	28.916732	0.3051	0.4594	1.05 ± 0.02	342.1 ± 2.8	0.81 ± 0.08	40.7 ± 1.33	0.28 ± 0.09	0.51 ± 0.19	4	F814W
J0955+0101	148.83217	1.02901	0.111	0.316	1.04 ± 0.06	238.4 ± 7.3	0.42 ± 0.11	8.73 ± 1.12	0.39 ± 0.07	0.67 ± 0.12	2	F450W
J1021+2028	155.435084	20.477728	0.1208	0.3507	0.49 ± 0.05	162.8 ± 8.1	0.35 ± 0.16	2.08 ± 0.41	1.25 ± 0.39	2.32 ± 1.02	4	F435W
J1029+0420	157.34560	4.33384	0.104	0.615	1.05 ± 0.03	211.7 ± 3.3	0.72 ± 0.15	6.54 ± 0.42	0.68 ± 0.13	1.19 ± 0.26	1	F814W
J1032+5322	158.14932	53.37636	0.133	0.329	1.06 ± 0.03	251.0 ± 3.3	0.58 ± 0.14	11.25 ± 0.56	0.46 ± 0.07	0.79 ± 0.13	2	F450W
J1037+3517	159.43764	35.29194	0.122	0.448	–	–	–	–	–	–	3	–
J1103+5322	165.78421	53.37450	0.158	0.735	1.08 ± 0.03	222.8 ± 3.1	0.49 ± 0.10	10.65 ± 0.65	0.61 ± 0.10	1.05 ± 0.17	2	F814W
J1111+2234	167.866760	22.580729	0.2223	0.9887	1.10 ± 0.01	227.9 ± 1.5	0.52 ± 0.07	14.95 ± 0.40	0.77 ± 0.20	1.37 ± 0.36	4	F435W
J1117+4704	169.39742	47.06873	0.169	0.405	0.77 ± 0.02	217.5 ± 2.5	0.59 ± 0.14	7.83 ± 2.16	0.61 ± 0.16	1.10 ± 0.32	3	F450W
J1135+3720	173.77867	37.33997	0.162	0.402	0.71 ± 0.07	206.3 ± 10.3	0.22 ± 0.10	6.14 ± 1.22	0.60 ± 0.16	1.11 ± 0.32	3	F435W
J1203+2535	180.98470	25.59697	0.101	0.856	0.87 ± 0.06	187.2 ± 5.9	0.80 ± 0.10	4.17 ± 0.50	0.68 ± 0.14	1.15 ± 0.20	3	F606W
J1251–0208	192.89877	–2.13477	0.224	0.784	0.82 ± 0.03	203.0 ± 2.6	0.74 ± 0.11	8.89 ± 0.46	0.47 ± 0.08	0.86 ± 0.11	1	F606W
J1313+0506	198.36127	5.11589	0.144	0.338	0.53 ± 0.23	172.2 ± 22.1	0.79 ± 0.16	2.91 ± 1.29	1.11 ± 0.54	1.86 ± 0.95	2	F606W
J1331+3638	202.91800	36.46999	0.113	0.254	0.96 ± 0.04	248.1 ± 4.4	0.67 ± 0.09	8.86 ± 0.61	0.38 ± 0.08	0.71 ± 0.16	3	F450W
J1422+4134	215.609046	41.576612	0.1011	3.01	1.18 ± 0.05	208.5 ± 4.3	0.73 ± 0.22	7.01 ± 0.58	0.13 ± 0.05	0.23 ± 0.08	4	F814W
J1703+2451	255.92278	24.86111	0.063	0.637	0.93 ± 0.05	189.7 ± 2.2	0.42 ± 0.08	2.91 ± 0.11	0.45 ± 0.06	0.84 ± 0.10	3	K p
J2141–0001	325.47781	–0.02008	0.138	0.713	0.88 ± 0.09	197.0 ± 11.0	0.48 ± 0.21	6.07 ± 1.34	0.67 ± 0.15	1.14 ± 0.26	2	F814W

Table 2. Summary of basic properties of the SWELLS *HST* cycle 18 targets. Column 1 lists the lens ID; columns 2 and 3 the coordinates (J2000 in degrees); columns 4 and 5 give deflector and source redshifts; column 6 the lens grade (A = secure, B = probable, C = possible and X = not a lens); column 7 the axis ratio as measured by SDSS; column 8 the reference for the discovery of the lens (3 = Paper I, 4 = this paper); column 9 the *HST* filters.

ID (1)	RA (2)	Dec. (3)	z_d (4)	z_s (5)	Grade (6)	q_{SDSS} (7)	Ref (8)	Filter(s) (9)
J0007+0053	1.886461	0.889701	0.2752	0.9119	X	0.54	4	F435W/F814W
J0028–0014	7.220414	–0.243334	0.1115	0.3103	C	0.53	4	F160W
J0149–0010	27.401391	–0.169114	0.2437	0.8263	C	0.57	4	F435W/F814W
J0329–0027	52.465504	–0.460612	0.2429	0.5117	B	0.53	4	F435W/F814W
J0745+3400	116.428559	34.007752	0.0647	0.2953	X	0.36	4	F160W
J0821+1025	125.48858	10.43226	0.0942	0.6568	C	–	3	F435W/F814W
J0822+1828	125.614474	18.482175	0.1153	0.8710	A	0.46	4	F435W/F814W
J0825+2109	126.320762	21.161022	0.1012	0.3956	X	0.26	4	F435W/F814W
J0908+2730	137.234813	27.513829	0.0219	0.2831	X	0.15	4	F160W
J0915+4211	138.81787	42.19800	0.078	0.790	A	0.59	3	F435W/F814W
J0930+2855	142.572560	28.916732	0.3051	0.4594	A	0.55	4	F435W/F814W
J1000+2835	150.011213	28.595699	0.0885	0.8757	X	0.41	4	F435W/F814W
J1021+2028	155.435084	20.477728	0.1208	0.3507	A	0.39	4	F435W/F814W
J1111+2234	167.866760	22.580729	0.2223	0.9887	A	0.58	4	F435W/F814W
J1135+3720	173.77867	37.33997	0.162	0.402	A	0.32	3	F435W/F814W
J1249+0225	192.467683	2.417972	0.0965	0.3517	C	0.43	4	F435W/F814W
J1403+1530	210.799017	15.511061	0.0976	1.0858	C	–	4	F435W/F814W/F160W
J1422+4134	215.609046	41.576612	0.1011	3.01	B	0.20	4	F435W/F814W
J1629+4708	247.291334	47.145309	0.1282	0.3739	B	0.41	4	F435W/F814W
J1633+1341	248.414833	13.687109	0.1171	0.2436	C	0.31	4	F435W/F814W
J2333–1042	353.272047	–10.703289	0.1445	0.1328	B	0.37	4	F435W/F814W

Table 3. Structure of SWELLS *HST* cycle 18 targets with multiband imaging. Column 1 lists the lens ID; columns 2–9 the AB magnitudes of the bulge and the disc in the various bands; column 10 circularized half-light radius of the bulge; column 11 the axis ratio of the bulge; column 12 circularized half-light radius of the disc; column 13 the axis ratio of the disc. The stellar masses inferred from these magnitudes are listed in Table 4.

ID	B_{bulge}	I_{bulge}	H_{bulge}	K_{bulge}	B_{disc}	I_{disc}	H_{disc}	K_{disc}	$R_{e,\text{bulge}}$ (arcsec)	q_{bulge}	$R_{e,\text{disc}}$ (arcsec)	q_{disc}
(1)	(2)	(3)	(4)	(5)	(6)	(7)	(8)	(9)	(10)	(11)	(12)	(13)
SDSS J0007+0053	21.79	19.12	—	—	21.79	19.72	—	—	0.45	0.68	1.40	0.39
SDSS J0149–0010	22.96	20.09	—	—	22.93	20.56	—	—	0.21	0.56	0.39	0.48
SDSS J0329–0027	22.68	19.63	—	—	21.91	19.52	—	—	0.16	0.85	0.90	0.39
SDSS J0821+1025	20.69	17.57	—	—	18.75	16.81	—	—	1.28	0.52	2.59	0.15
SDSS J0822+1828	19.86	17.50	—	—	20.51	18.40	—	—	0.65	0.66	1.09	0.24
SDSS J0825+2109	48.84	20.35	—	—	18.80	16.99	—	—	0.32	0.79	1.80	0.24
SDSS J0915+4211	19.02	16.82	—	15.63	19.55	17.68	—	16.73	1.05	0.89	1.40	0.25
SDSS J0930+2855	21.53	18.28	—	—	21.97	18.95	—	—	0.62	0.53	2.36	0.75
SDSS J1000+2835	19.56	17.32	—	—	19.61	17.71	—	—	0.58	0.79	1.43	0.20
SDSS J1021+2028	19.75	17.42	—	—	20.82	19.13	—	—	0.40	0.44	0.70	0.17
SDSS J1111+2234	20.33	17.62	—	—	19.94	17.84	—	—	0.71	0.67	1.38	0.46
SDSS J1135+3720	21.37	18.45	—	17.19	19.91	17.54	—	16.45	0.56	0.67	1.41	0.26
SDSS J1249+0225	20.31	18.08	—	—	19.78	17.84	—	—	0.37	0.73	1.06	0.32
SDSS J1403+1530	20.95	18.16	16.88	—	18.98	17.02	16.34	—	0.60	0.62	1.97	0.36
SDSS J1422+4134	48.24	19.69	—	—	18.64	16.78	—	—	0.54	0.57	2.06	0.16
SDSS J1629+4708	20.17	17.80	—	—	19.64	17.56	—	—	0.39	0.71	1.16	0.25
SDSS J1633+1341	21.90	19.29	—	—	19.69	17.38	—	—	0.91	0.15	2.07	0.26
SDSS J2333–1042	20.40	16.97	—	—	19.48	17.13	—	—	1.23	0.65	1.32	0.18

Table 4. Stellar mass estimates for the SWELLS *HST* cycle 18 targets with multiband imaging. Column 1 lists the lens ID; columns 2 and 3 the stellar masses of the bulge and disc assuming a Chabrier (2003) IMF; columns 4 and 5 the stellar masses of the bulge and disc assuming a Salpeter (1955) IMF.

ID	$\log_{10}(M_{*,\text{bulge}}/\text{M}_\odot)$ Chabrier	$\log_{10}(M_{*,\text{disc}}/\text{M}_\odot)$ Chabrier	$\log_{10}(M_{*,\text{bulge}}/\text{M}_\odot)$ Salpeter	$\log_{10}(M_{*,\text{disc}}/\text{M}_\odot)$ Salpeter
(1)	(2)	(3)	(4)	(5)
SDSS J0007+0053	10.63 ± 0.14	10.26 ± 0.11	10.84 ± 0.18	10.43 ± 0.13
SDSS J0149–0010	10.21 ± 0.16	9.90 ± 0.14	10.57 ± 0.19	10.21 ± 0.13
SDSS J0329–0027	10.44 ± 0.14	10.26 ± 0.17	10.72 ± 0.15	10.57 ± 0.15
SDSS J0821+1025	10.40 ± 0.11	10.60 ± 0.13	10.64 ± 0.11	10.78 ± 0.16
SDSS J0822+1828	10.54 ± 0.13	10.09 ± 0.11	10.79 ± 0.16	10.34 ± 0.16
SDSS J0825+2109	—	10.58 ± 0.17	—	10.81 ± 0.16
SDSS J0915+4211	10.60 ± 0.11	10.17 ± 0.10	10.83 ± 0.09	10.43 ± 0.09
SDSS J0930+2855	11.18 ± 0.15	10.85 ± 0.15	11.42 ± 0.17	11.11 ± 0.17
SDSS J1000+2835	10.40 ± 0.14	10.18 ± 0.14	10.57 ± 0.17	10.34 ± 0.14
SDSS J1021+2028	10.62 ± 0.13	9.74 ± 0.14	10.87 ± 0.18	9.98 ± 0.12
SDSS J1111+2234	11.11 ± 0.13	10.88 ± 0.15	11.37 ± 0.14	11.10 ± 0.15
SDSS J1135+3720	10.62 ± 0.08	10.91 ± 0.10	10.85 ± 0.09	11.09 ± 0.07
SDSS J1249+0225	10.15 ± 0.13	10.16 ± 0.13	10.32 ± 0.16	10.50 ± 0.15
SDSS J1403+1530	10.33 ± 0.10	10.51 ± 0.12	10.58 ± 0.12	10.76 ± 0.10
SDSS J1422+4134	—	10.56 ± 0.17	—	10.84 ± 0.15
SDSS J1629+4708	10.52 ± 0.12	10.49 ± 0.15	10.73 ± 0.16	10.78 ± 0.12
SDSS J1633+1341	9.88 ± 0.14	10.67 ± 0.15	10.11 ± 0.13	10.84 ± 0.20
SDSS J2333–1042	11.08 ± 0.13	10.86 ± 0.14	11.29 ± 0.12	11.07 ± 0.15

$a_y(x, y) = \frac{b\sqrt{q}}{\sqrt{1-q^2}} \tanh^{-1} \left[\frac{y\sqrt{1-q^2}}{\psi + q^2} \right]$,
as long as $q < 1$. If $q > 1$, then q can simply be replaced by q^{-1} and the orientation angle θ rotated by 90° , with the same result. We do not allow $q = 1$, but it can become arbitrarily close to 1 and therefore close-to-spherical lenses are not ruled out. The parameter b denotes the Einstein radius of the lens, using the intermediate-axis convention.

In many cases, we are attempting to fit this lens model to image data that do not contain very much information. Therefore, informative priors on the lens model parameters are required. The centre of the lens model is fixed to be within ± 3 pixels of the peak pixel of the light distribution. The position angle of the lens model is assigned an informative prior, stating that the position angle of the lens is likely to be within $\pm 10^\circ$ of the position angle of the lens galaxy light. The modelling results in an (intermediate axis) Einstein radius b and an ellipticity parameter q for each system. Once the lens model parameters have been estimated, the Einstein

Table 5. Stellar mass-to-light ratios, in solar units [i.e. $(M/M_{\odot})/(L/L_{\odot})$], for the SWELLS *HST* cycle 18 targets with multiband imaging. Column 1 lists the lens ID; columns 2–5 the mass-to-light ratio of the bulge and disc in the B and V bands assuming a Chabrier (2003) IMF; columns 6–9 the mass-to-light ratio of the bulge and disc in the B and V bands assuming a Salpeter (1955) IMF.

ID (1)	$(M/L)_B$ Bulge Chabrier (2)	$(M/L)_V$ Bulge Chabrier (3)	$(M/L)_B$ Disc Chabrier (4)	$(M/L)_V$ Disc Chabrier (5)	$(M/L)_B$ Bulge Salpeter (6)	$(M/L)_V$ Bulge Salpeter (7)	$(M/L)_B$ Disc Salpeter (8)	$(M/L)_V$ Disc Salpeter (9)
SDSS J0007+0053	2.37 ± 0.70	2.02 ± 0.50	1.37 ± 0.33	1.35 ± 0.28	3.98 ± 1.54	3.38 ± 1.03	2.05 ± 0.55	2.06 ± 0.45
SDSS J0149–0010	3.36 ± 1.07	2.65 ± 0.71	2.01 ± 0.58	1.76 ± 0.40	7.40 ± 3.00	5.58 ± 1.82	4.02 ± 1.12	3.55 ± 0.78
SDSS J0329–0027	3.38 ± 0.95	2.66 ± 0.61	1.65 ± 0.65	1.55 ± 0.51	6.62 ± 2.06	5.14 ± 1.28	3.28 ± 1.02	2.94 ± 0.74
SDSS J0821+1025	6.48 ± 1.73	4.52 ± 1.05	2.92 ± 0.91	2.44 ± 0.64	11.66 ± 2.79	8.20 ± 1.67	4.49 ± 1.78	3.82 ± 1.18
SDSS J0822+1828	3.45 ± 1.14	2.75 ± 0.73	2.48 ± 0.68	2.19 ± 0.47	6.30 ± 2.28	5.04 ± 1.45	4.49 ± 1.70	3.80 ± 1.14
SDSS J0825+2109	–	–	2.43 ± 1.01	2.11 ± 0.67	–	–	4.16 ± 1.54	3.62 ± 1.05
SDSS J0915+4211	5.16 ± 1.40	3.82 ± 0.87	3.54 ± 0.97	2.84 ± 0.63	8.45 ± 2.11	6.39 ± 1.33	6.41 ± 1.58	5.10 ± 1.05
SDSS J0930+2855	3.70 ± 1.03	2.84 ± 0.65	3.01 ± 0.88	2.37 ± 0.55	6.55 ± 2.18	4.98 ± 1.35	5.54 ± 1.83	4.38 ± 1.17
SDSS J1000+2835	4.12 ± 1.33	3.16 ± 0.82	2.98 ± 0.99	2.47 ± 0.67	6.33 ± 2.69	4.97 ± 1.69	4.36 ± 1.49	3.74 ± 1.00
SDSS J1021+2028	3.65 ± 1.04	2.85 ± 0.64	1.69 ± 0.61	1.60 ± 0.45	6.59 ± 2.66	5.19 ± 1.72	2.91 ± 0.73	2.77 ± 0.59
SDSS J1111+2234	3.23 ± 0.85	2.56 ± 0.54	1.87 ± 0.60	1.71 ± 0.45	5.97 ± 2.00	4.71 ± 1.27	3.08 ± 0.88	2.77 ± 0.62
SDSS J1135+3720	5.63 ± 1.16	4.05 ± 0.73	3.72 ± 0.91	2.92 ± 0.62	9.51 ± 2.24	6.86 ± 1.41	5.46 ± 1.10	4.41 ± 0.73
SDSS J1249+0225	3.74 ± 1.11	2.99 ± 0.70	2.53 ± 0.85	2.20 ± 0.57	5.49 ± 2.08	4.47 ± 1.34	5.65 ± 1.92	4.60 ± 1.25
SDSS J1403+1530	7.25 ± 1.85	5.00 ± 1.12	2.66 ± 0.72	2.25 ± 0.48	13.20 ± 4.08	9.06 ± 2.43	4.65 ± 1.18	3.90 ± 0.83
SDSS J1422+4134	–	–	2.22 ± 0.92	1.96 ± 0.63	–	–	4.28 ± 1.55	3.65 ± 1.07
SDSS J1629+4708	3.58 ± 1.01	2.83 ± 0.64	2.42 ± 0.81	2.06 ± 0.56	5.97 ± 2.03	4.72 ± 1.33	4.57 ± 1.22	3.88 ± 0.85
SDSS J1633+1341	4.17 ± 1.24	3.18 ± 0.76	3.83 ± 1.21	2.97 ± 0.76	7.14 ± 2.10	5.48 ± 1.30	5.80 ± 2.41	4.61 ± 1.55
SDSS J2333–1042	7.13 ± 1.99	4.92 ± 1.21	3.11 ± 0.95	2.51 ± 0.61	11.80 ± 3.38	8.20 ± 2.03	5.13 ± 1.73	4.21 ± 1.14

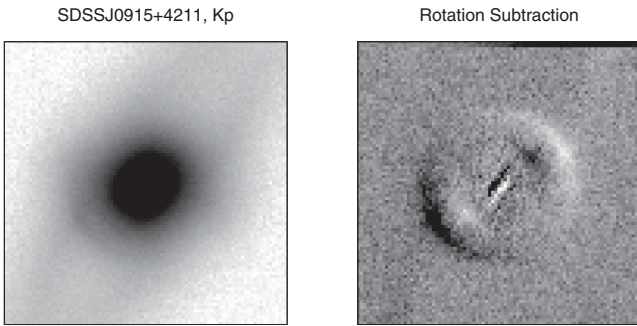


Figure 3. Rotation subtraction for the K_p image of the SWELLS system SDSS J0915+4211. The lensed arc and counter-image are revealed by this process. The rotation-subtracted image is then used to mask the image so that a proper multi-Gaussian fit can be made.

radius in radians can be converted to an equivalent velocity dispersion σ_{SIE} using

$$\sigma_{\text{SIE}} = c \sqrt{\frac{b}{4\pi}} \times \sqrt{\frac{D_s}{D_{ds}}}, \quad (4)$$

where D_s and D_{ds} are the angular diameter distances (Hogg 1999) from the observer to the source and the deflector to the source, respectively. For simplicity, we modelled the sources with a single circular Gaussian component as this is adequate to explain the observed lensing configuration in most cases. For those cases where this model was inadequate, the source was generalized to be either an elliptical Gaussian (e.g. for J0820+4847) or multiple spherical Gaussians (e.g. for J0822+1828). Due to the presence of systematics in the data from incomplete subtraction of lens galaxy light, and also the simplicity of the model used, we do not literally perform the inference with the Brewer et al. (2011a) likelihood $\mathcal{L}(\theta)$, as this would result in inappropriately small uncertainties on the inferred

quantities due to the systematic errors. Simple, commonly adopted models for the likelihood function tend to assume that the measurement error in each pixel is independent and that measurement error is the sole cause of discrepancies between the model and the data. This is not true in the presence of significant systematic effects such as residuals from an incomplete lens galaxy subtraction, and the assumption of a specific form (Gaussian) for the source light profile.

To account for this and obtain realistic uncertainties on b and q despite the use of a simplified model, we adopted the following strategy. This strategy has previously been briefly discussed by Brewer et al. (2011a,c) and will be presented in depth in a forthcoming contribution (Brewer et al., in preparation).

We carry out the sampling of the posterior distribution for the lens model parameters using a nested sampling algorithm (Skilling 2006; Brewer, Pártay & Csányi 2011b). Rather than simply sampling the posterior distribution (which would yield unrealistic small uncertainties due to the presence of systematics and the simplified model), we explore the dependence of the posterior distribution for the parameters θ on the temperature T :

$$p(\theta|D; T) \propto \pi(\theta) \mathcal{L}(\theta)^{1/T}, \quad (5)$$

where θ denotes the parameters of the lens model, $\pi(\theta)$ is the prior and $\mathcal{L}(\theta)$ is the standard likelihood function. The temperature controls how conservative the posterior distribution is: $T = \infty$ reproduces the prior and $T = 1$ gives the standard posterior obtained by ignoring the systematics.

For each system, we then choose the highest temperature T for which the posterior distribution over predicted lensed images (the third panel in Fig. 4) matches the gross lensed features seen in the data. In other words, we force the posterior distribution to be as conservative as possible while still fitting the morphological features of the lensed images that are believed to be robust. Note that using a temperature T is analogous to increasing the noise standard deviations on the data by a factor \sqrt{T} . This procedure does not change

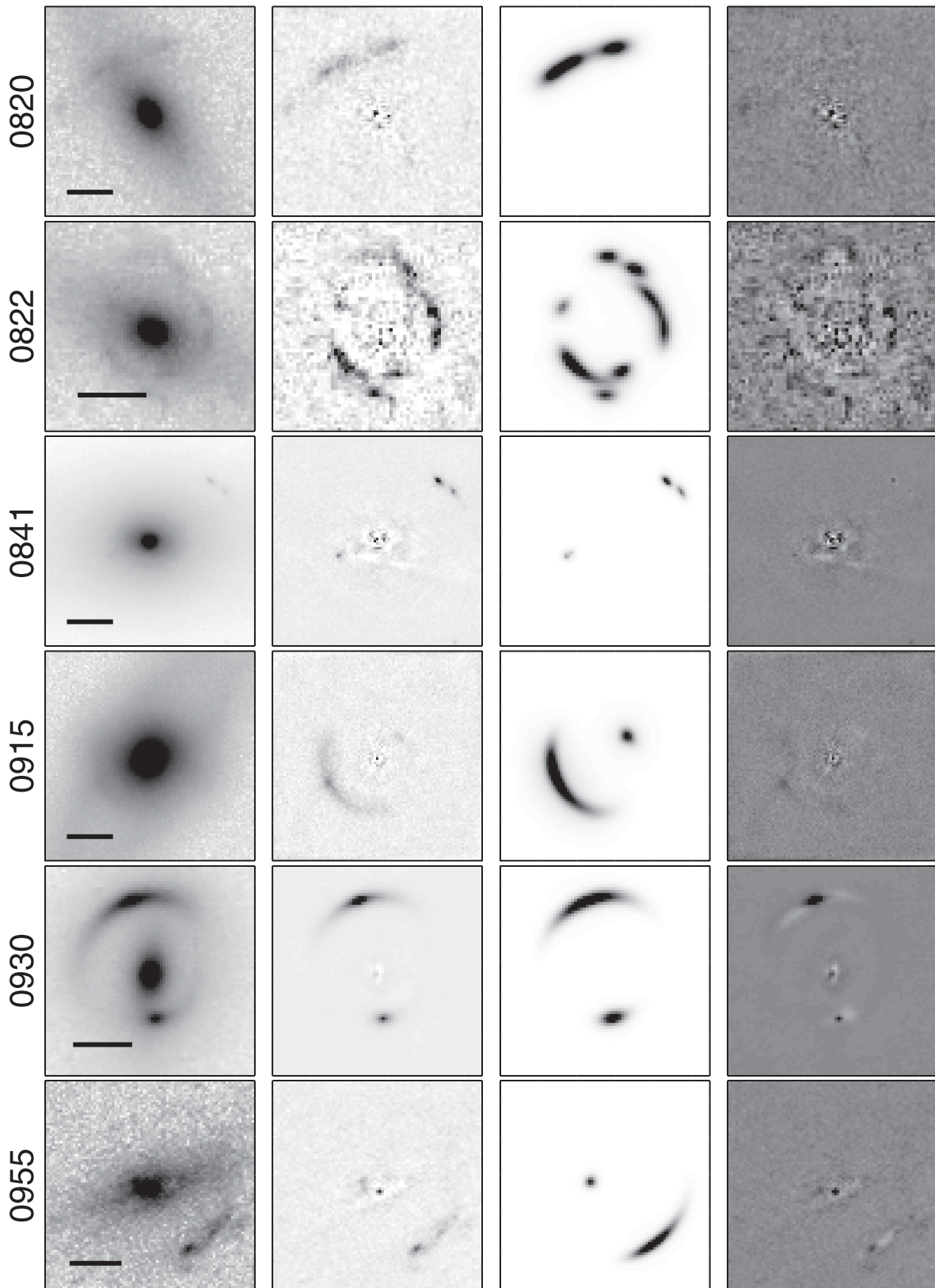


Figure 4. Images and gravitational lens models of SWELLS systems. Left to right: image, lens-subtracted image, lens model-predicted image (for a model chosen at random from the posterior distribution) and residuals of lens model fit. The black bar in the left-hand panel has a length of 1 arcsec.

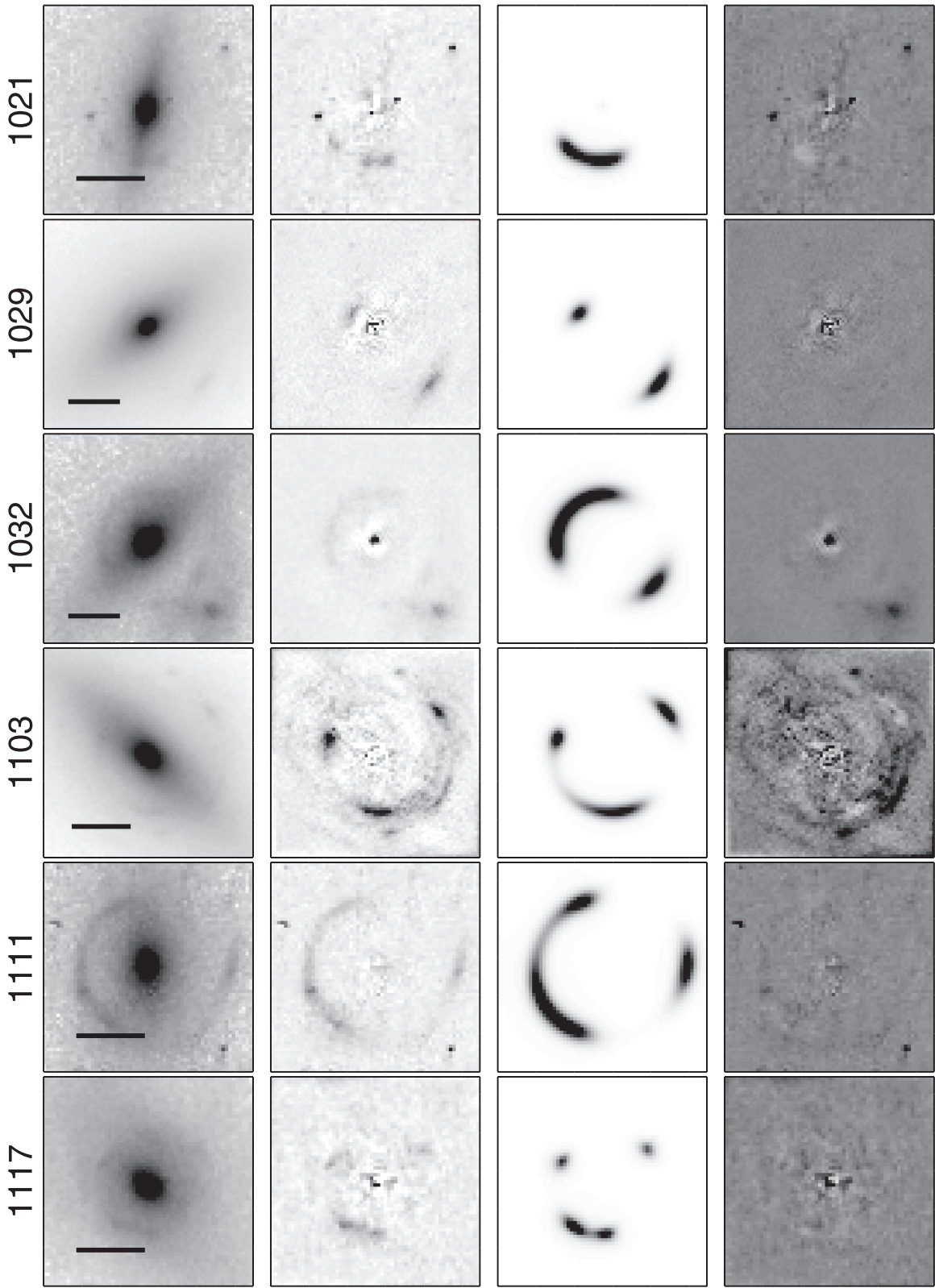
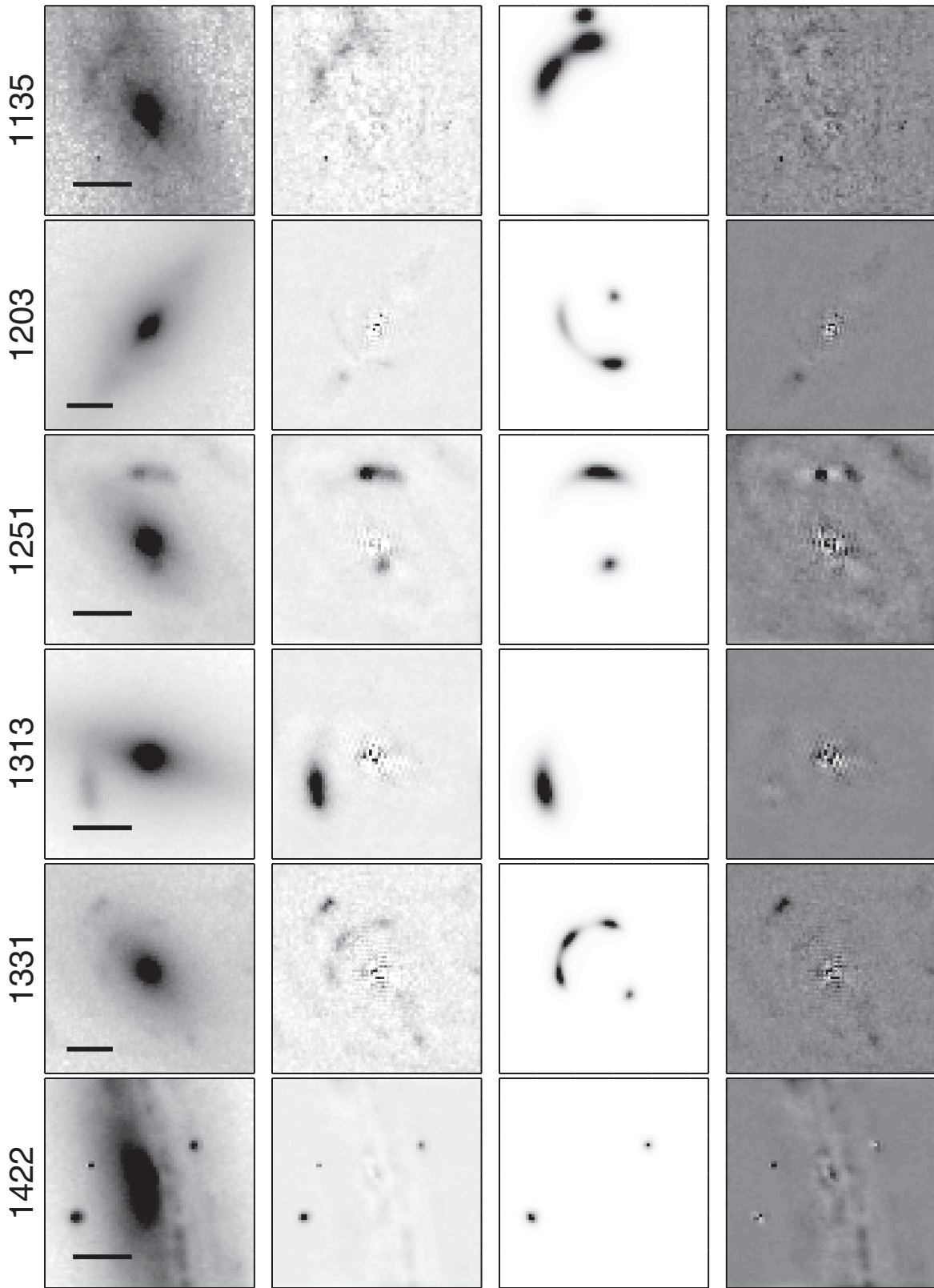


Figure 4 – continued

the values of our best estimates for the lens model parameters, but does increase the uncertainty around these estimates. Not carrying out this procedure would result in substantially underestimated uncertainties.

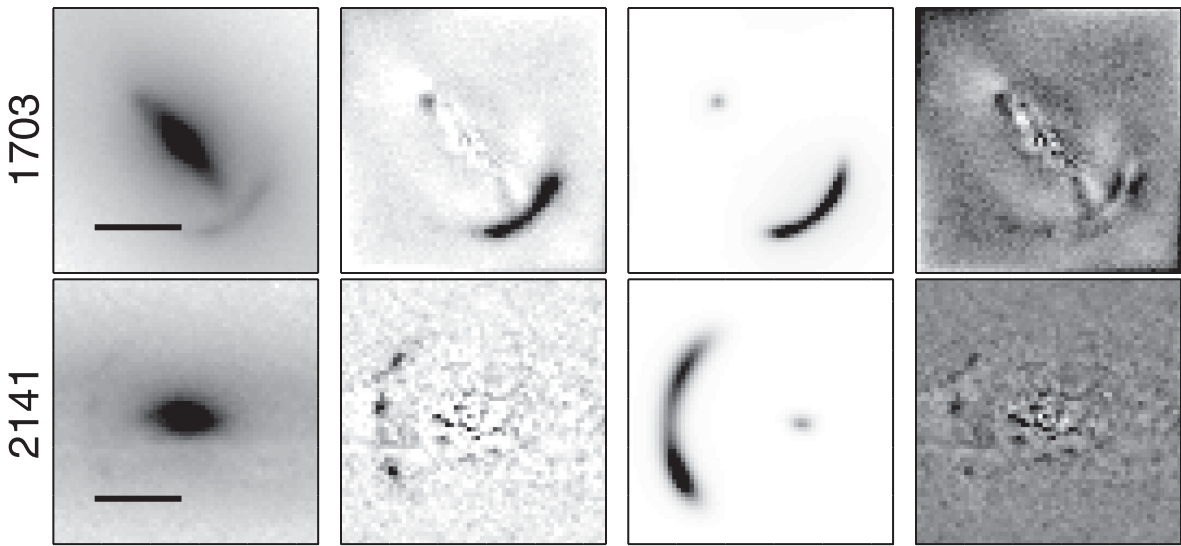
See Fig. 4 for images of the lenses, along with galaxy-subtracted images, lens models (chosen at random from the posterior distribution) and the residuals of the lens model fits. In several cases there are significant residuals remaining after the

**Figure 4 – *continued***

fitting procedure; these are generally due to the source having more structure than the surface brightness model that was assumed. In all cases the lensing aperture mass estimates are reliable.

3.3 Notes on individual systems

In this section we give brief notes on the image configurations of the lens models.

Figure 4 – *continued*

0820+4847. Very little curvature is present in the arc. No definite counter-image is detected. An elliptical source is required, and the deflector is inferred to be very flat.

0822+1828. Multiple (three) source components are required. This results in tight constraints on the lens model parameters.

0841+3824. Two source components are required. Whereas a bimodal posterior PDF is found, one mode is chosen because of unrealistic small axis ratios for the other modes. A consistent lens model for this system has also been presented by B08.

0915+4211. Straightforward fit of the arc and counter-image with a single circular source.

0930+2855. Significant residuals due to the assumptions of no shear and isothermality (Auger et al., in preparation). The source has very high surface brightness and the system is an example of an early-type/early-type lensing system (e.g. Auger et al. 2011).

0955+0101. Straightforward fit of arc and counter-image with a double image configuration. A consistent lens model for this system has also been presented by B08.

1021+2028. We fit to the arc only. A bimodal solution was found, but we could rule out the mode which did predict a distant unseen counter-image.

1029+0420. Classic double image configuration. A consistent lens model for this system has also been presented by B08.

1032+5322. Arc and counter-image are well modelled by a single circular source. A consistent lens model for this system has also been presented by B08.

1103+5322. Arc can be explained by a single circular source imaged four times. Lens model parameters are tightly constrained. A consistent lens model for this system has also been presented by B08.

1111+2234. Arc can be explained by a single circular source imaged four times. Lens model parameters are tightly constrained.

1117+4704. The single circular source is lensed into a quad configuration. Lens model parameters are tightly constrained.

1135+3720. The arc structure is complex, requiring two components for a good fit. Position of the counter-image is uncertain. Lens parameter constraints are not particularly tight.

1203+2535. Position and morphology of the arc can be reproduced by a single circular source. Subtraction of the deflector galaxy

was not straightforward for this system, leaving residuals that may add systematic uncertainties.

1251-0208. Classic double image configuration. A consistent lens model for this system has also been presented by B08.

1313+0506. Arc is well matched by a lensed circular source, but due to the non-detection of a counter-image, the constraints on the lens model parameters are weak.

1331+3638. Classic cusp configuration leads to strong constraints on the lens model parameters.

1422+4134. This is the only grade ‘B’ lens system for which a plausible model has currently been obtained. The two compact images are possibly double images of a background quasar. This configuration yields weak constraints on the lens model, and the inferred stellar mass fractions place this system as a significant outlier from the relation in Fig. 5, possibly due to its significant dust content or a potential misidentification of the source redshift. Hence, this system has been excluded from the IMF analysis of Section 4.

1703+2451. Arc and counter-image can be explained by a single circular source.

2141-0001. As discussed in Paper II, the arc appears to be split into three images, but this is likely due to the presence of two dust lanes. The arc morphology can be explained by a single circular source. The posterior distribution includes models where the arc is split into distinct images, as well as models where the arc is continuous.

4 COMPARING STELLAR MASS AND LENSING MASS

In this section we derive lensing and stellar masses within the critical curves (Section 4.1), and compare them to derive limits on the stellar in IMF (Section 4.2).

4.1 Lensing and stellar masses within the critical curves

As in Paper I, we fit the surface brightness models to the available high-resolution imaging, i.e. the *HST* and Keck-AO imaging, using the multicolour fitting code SPASMOID (Bennert et al. 2011). The stel-

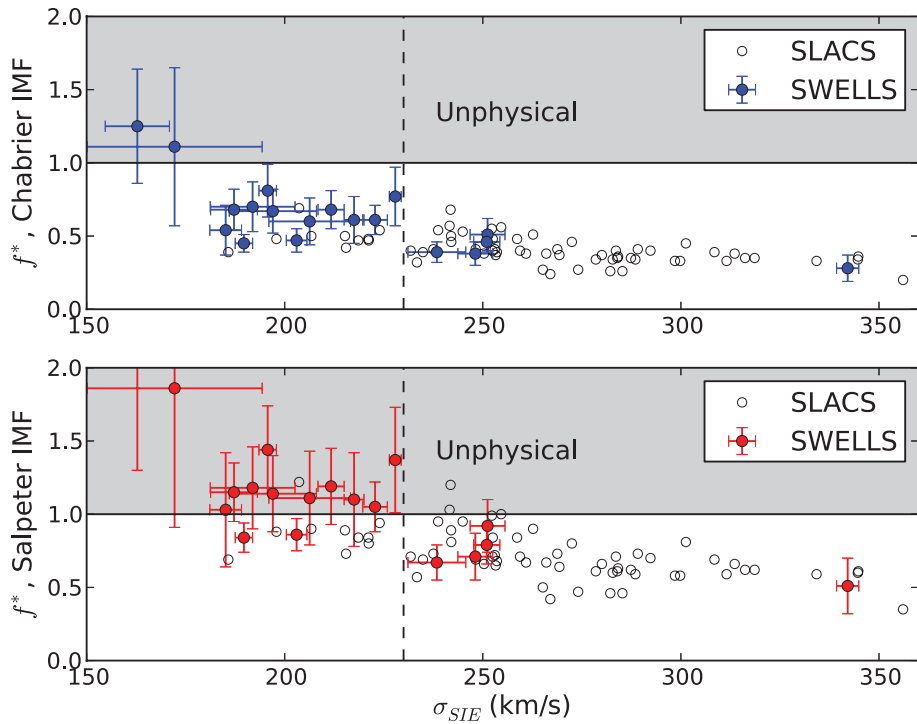


Figure 5. Stellar mass fraction within the critical curve versus lensing velocity dispersion for the SWELLS sample. The SLACS sample (with duplicates in SWELLS removed) (Auger et al. 2009) is also plotted for comparison. Note that, at the low-mass end (to the left of the dashed line at $\sigma_{\text{SIE}} < 230 \text{ km s}^{-1}$), the Salpeter IMF assumption results in inferred stellar mass fractions greater than unity, which is unphysical.

lar mass (and surface brightness) model consists of an $n = 4$ Sérsic profile (i.e. a de Vaucouleurs profile) for the bulge and an $n = 1$ exponential disc component. One advantage of SPASMOID over similar methods such as GALFIT (Peng et al. 2002) is the ability to take into account prior information such as the fact that the disc component should have a larger effective radius and a higher ellipticity than the bulge. Once we have obtained the surface photometry parameters, we infer the stellar masses of the bulge and disc components using a Bayesian method for fitting SPS models to multiband photometric data (Auger et al. 2009). This method uses a grid of models output from a standard SPS code, and allows for marginalization over unknown parameters such as star formation history, metallicity, etc. A summary of the structural properties (stellar masses, sizes and axis ratios) of the SWELLS cycle 18 targets with multiband imaging is given in Tables 3 and 4. For the other lenses we use the structural parameters as reported in Paper I.

We then integrate these models to obtain the total stellar mass $M_{*,\text{SPS}}$ within the critical curve. This can be compared with the inferred mass within the critical curve from lensing (M_{lens}), yielding stellar mass fractions $f^* = M_{*,\text{SPS}}/M_{\text{lens}}$ under both the Chabrier IMF assumption and the Salpeter IMF assumption. The reason for the choice of the critical curve as the integration aperture is that, heuristically, it is the aperture within which the mass of the lens is most strongly constrained (e.g. Treu 2010, and references therein). To obtain uncertainties on the stellar mass fractions, we Monte Carlo sample from the posterior distribution for the lens model parameters and the posterior distributions for the total stellar mass.

The resulting stellar mass fractions for the grade ‘A’ lenses, under the Chabrier and Salpeter assumptions, are plotted in Fig. 5 as a function of lensing velocity dispersion (a proxy for overall galaxy mass that can be measured accurately and independent of the size of the Einstein radius and the normalization of the stellar IMF).

Remarkably, there is a smooth declining trend as a function of stellar velocity dispersion over more than a factor of 2 in stellar velocity dispersion (and a factor of ~ 10 in stellar mass). This trend can be due to two effects: (i) a systematic variation of the IMF; and (ii) a varying dark matter fraction within the Einstein radius due to a change in stellar mass-to-dark matter ratio and the change in physical size of the Einstein radius. Disentangling the two effects is a major goal of the SWELLS survey and requires very realistic lensing and dynamical models (e.g. Paper II). However, as we will show in the rest of this paper, a very robust inference on the normalization of the IMF at the low velocity dispersion end can be obtained based on a very simple argument.

At the low velocity dispersion end, the Salpeter IMF assumption results in inferred stellar mass fractions greater than unity, which is clearly unphysical, especially considering that there may be an additional contribution of cold gas distributed as the stars (Paper II and references therein). This provides evidence against the Salpeter IMF and any IMF that would predict a similar or greater stellar mass. In Section 4.2 we formalize this argument with a probabilistic model and derive quantitative constraints on the IMF for the lower mass ($\sigma_{\text{SIE}} < 230 \text{ km s}^{-1}$) SWELLS galaxies.

4.2 Constraints on the initial mass function

Our data do not allow us to probe the form of the IMF, but they do allow us to place robust constraints on the integral of the IMF: if the assumed IMF yields a mass significantly greater than the inferred total mass from lensing (i.e. a stellar mass fraction much greater than unity), then this IMF is excluded by our data. We could assume that all of our galaxies have the same underlying central stellar mass fraction f_{true}^* , in which case the estimate for a Salpeter IMF (i.e. the variance-weighted mean of the points in Fig. 5) would imply

$f_{\text{true}}^* > 1$. However, there is certainly some amount of scatter in the central dark matter fraction and therefore in the stellar mass fraction. We therefore explicitly build a model for the true underlying stellar mass fraction that includes Gaussian scatter and the fact that f_{true}^* is between 0 and 1. In practice, this is a truncated normal distribution, which we parametrize as having a peak at μ and characteristic width σ . Then the probability of observing a set of galaxies with true stellar mass fractions $\{F_i^*\}$ is given by

$$p(\{F_i^*\}|\mu, \sigma) = \prod_{i=1}^n \frac{\exp\left[-\frac{1}{2\sigma^2}(F_i^* - \mu)^2\right]}{\int_0^1 \exp\left[-\frac{1}{2\sigma^2}(F_i^* - \mu)^2\right] dF_i^*}, \quad (6)$$

where $F_i^* \equiv f_{\text{true},i}^* \in [0, 1]$. We also introduce a parameter α that parametrizes the difference between a true (unknown) normalization of the IMF and the normalization resulting from a Salpeter IMF:

$$M_{*,\text{true}} = \alpha M_{*,\text{Salp}}.$$

This normalization is always greater than 0, and $\alpha = 1$ implies a Salpeter IMF (a Chabrier IMF typically would imply $\alpha \sim 0.55$). At fixed total mass, an increase in α yields an increase in f_{true}^* , demonstrating that the parameters are highly degenerate. However, as noted previously, α cannot be raised to arbitrarily large values because the stellar mass fraction is bounded to be less than unity. In practice, α plays a similar role to a stellar mass-to-light ratio but has the benefit of being less dependent on dust and age due to having explicitly modelled the spectral energy distributions of the galaxies (see Section 4.1).

Given our data – total masses from lensing and stellar masses assuming a Salpeter-like normalization of the IMF – and invoking Bayes' theorem allow us to write down the probability distribution for our unknown model parameters μ , σ , α and $\{F_i^*\}$, given the data:

$$\begin{aligned} p(\alpha, \mu, \sigma, \{F_i^*\} | \{f_i^*\}) &\propto p(\alpha, \mu, \sigma, \{F_i^*\}) \\ &\times p(\{f_i^*\} | \alpha, \mu, \sigma, \{F_i^*\}) \\ &= p(\alpha)p(\mu)p(\sigma) \\ &\times p(\{F_i^*\} | \mu, \sigma)p(\{f_i^*\} | \{F_i^*\}), \end{aligned} \quad (7)$$

where $f_i^* = \alpha f_{i,\text{Salp}}^*$ are the scaled observed stellar mass fraction, $\{F_i^*\}$ is the set of true (unknown) stellar mass fractions and the leading terms are priors on α , μ and σ . The term $p(\{F_i^*\} | \mu, \sigma)$ is given by equation (6) and the term $p(\{f_i^*\} | \{F_i^*\})$ is the likelihood of having observed the data, taken to be a multivariate normal distribution with means $\{F_i^*\}$ and standard deviations given by the measurement uncertainties (the galaxies are independent and there are therefore no covariances).

The inferences on the parameters (μ, σ, α) were computed using Markov chain Monte Carlo, with the true F^* explicitly integrated out:

$$p(\alpha, \mu, \sigma, \{f_i^*\}) = \int p(\alpha, \mu, \sigma, \{F_i^*\} | \{f_i^*\}) d^n F_i^*. \quad (9)$$

These inferences were calculated assuming a uniform prior on μ (a location parameter) between 0 and 1, a log-uniform prior on σ (a scale parameter) between 0.01 and 1, and a log-uniform prior on α (a scale parameter) between 0.2 and 5, all independent. The results are shown in Figs 6 and 7. Values of α less than about 0.9 are approximately equally plausible, but the evidence strongly disfavours values of α greater than unity. The evidence for the point hypothesis $\alpha = 0.5$ is only about twice that of the point hypothesis $\alpha = 1$; however, the probability that the IMF is lighter than Salpeter is 98 per cent. This result depends slightly on the chosen prior for

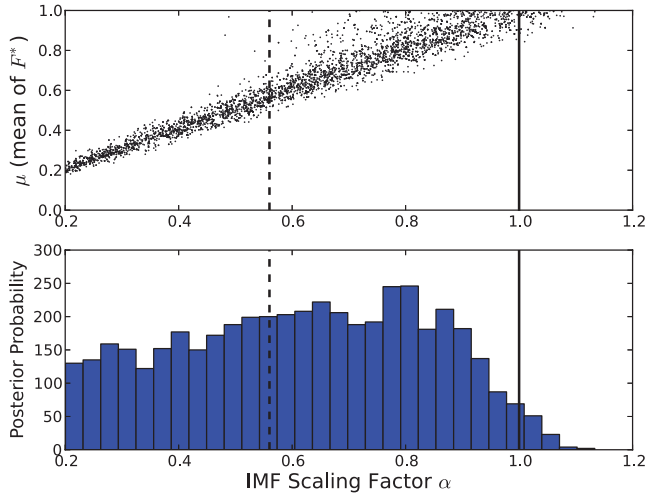


Figure 6. Inference on the IMF mismatch parameter α and the parameter μ , the mean of the true distribution of stellar mass fractions. Values of α less than about 0.9 are approximately equally plausible, but the evidence strongly disfavours higher values of α . The vertical line denotes the Salpeter IMF, and the dashed line indicates a Chabrier-like (in terms of mass-to-light ratio) IMF. The probability that the IMF is lighter than Salpeter is 98 per cent.

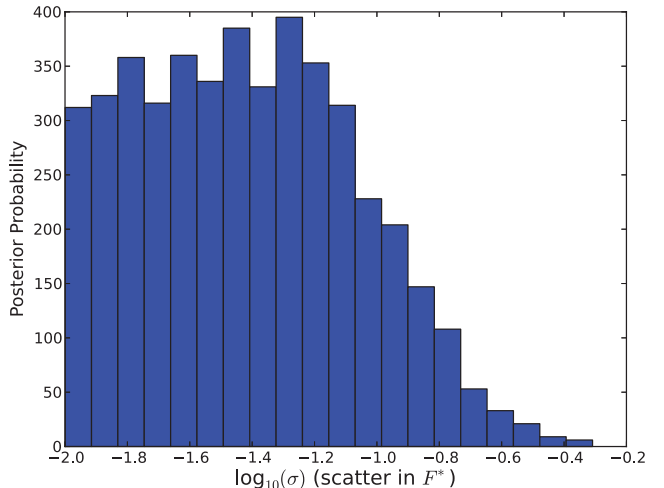


Figure 7. Inference on the parameter σ , the intrinsic scatter in the true distribution of stellar mass fractions F^* . The value of σ is constrained to be low (<0.16 with 95 per cent probability), so there is evidence that the intrinsic stellar mass fractions are fairly homogeneous across the low-mass end of the SWELLS sample.

μ , α and σ , and becomes weaker if a greater prior probability is implicitly assigned to the hypothesis that the intrinsic F^* values are clustered close to 1. For example, if the prior bounds on μ are extended to -0.1 and 1.1 , allowing the true F^* distribution to place most of its mass near 1, the posterior probability that the IMF is lighter than Salpeter is slightly reduced to 93 per cent. The intrinsic scatter on the true F^* values is inferred to be small ($\sigma < 0.16$ with 95 per cent probability).

Note that, if we take into account the fact that there can be an additional 20 per cent of mass in cold gas distributed in the same way as the stars (as in Papers II), the probability that the IMF is lighter than Salpeter becomes greater than 99 per cent. Correspondingly, the 95 per cent probability upper limit to α becomes 0.80.

5 DISCUSSION AND COMPARISON WITH PREVIOUS WORK

The main result of this paper is that the stellar mass of spiral galaxies with lens velocity dispersion between 160 and 230 km s⁻¹ (i.e. with masses comparable to or slightly above the Milky Way) is lighter than that predicted based on their colours using a Salpeter IMF.

This conclusion is based on a robust and straightforward argument, i.e. the stellar mass cannot exceed the total mass measured by strong gravitational lensing. A high abundance of cold gas would make our result even stronger, requiring even less mass in stars and therefore a lighter normalization of the IMF. Systematic uncertainties in the stellar mass estimates due to differences in SPS models and assumptions are of the order of 0.05–0.1 dex for a fixed IMF (Auger et al. 2009; Conroy et al. 2009; Treu et al. 2010) and therefore not sufficient to modify our conclusions significantly.

Even though our sample is the largest sample of spiral lens galaxies currently available, it is important to consider whether this result could somehow be biased by unknown selection effects. In Paper I we investigated the selection function in detail by comparing the size mass relation of SWELLS lenses to that of non-lens galaxies selected from SDSS and found them to be statistically equivalent. The detailed analysis of the lens SDSS J2141–0001 presented in Paper II indicates that that galaxy might be drawn from the densest part of the distribution of mass density profiles of spiral galaxies. Whether this is a generic feature of lensing selection needs to be verified by the detailed analysis of the entire sample. However, if lens galaxies were representative of the densest spiral galaxies, this would only make our inference stronger with respect to the overall population, since the densest galaxies are likely those with the highest stellar content.

Our results are consistent with independent estimates of the normalization of the stellar IMF of spiral galaxies based on a variety of techniques. For example, based on spiral galaxy rotation curves, Bell & de Jong (2001) find that a Salpeter IMF is too heavy and argue for a normalization that is significantly lower. Based on the vertical velocity dispersion of discs, the Disc Mass Survey (Bershady et al. 2011, 2010) argues that the mass-to-light ratio (and hence the normalization of the stellar IMF) is significantly lower than that inferred assuming a Salpeter IMF. Interestingly, a qualitatively similar result is found for elliptical galaxies in the same velocity dispersion range. Dynamical arguments (Cappellari et al. 2006; Dutton et al. 2012) as well as joint dynamical and lensing arguments (Barnabè et al. 2010, 2011) show that a Salpeter IMF is too heavy for low-mass ellipticals.

The light normalization of the stellar IMF (or equivalently mass-to-light ratio) required for spirals and ellipticals comparable to the mass of the Milky Way is in contrast to the heavier normalization required for more massive systems. For example, van Dokkum & Conroy (2010), Spiniello et al. (2011), Auger et al. (2010b) and Sonnenfeld et al. (2011), using different techniques and data sets, find that light Chabrier-like IMFs are ruled out for the most massive early-type galaxies, and a heavier IMF is preferred. Further evidence for this hypothesis is provided by Treu et al. (2010) and Thomas et al. (2011) – and Newman et al. (2011) for the case of massive brightest cluster galaxies – although those studies could not break completely the degeneracy between dark matter content and normalization of the IMF.

Taken together, these results are consistent with the hypothesis that the stellar IMF is not universal, but that it changes sys-

tematically with galaxy stellar velocity dispersion and mass (and therefore halo mass to first approximation). Since stellar velocity dispersion correlates with the age of the stellar populations, this non-universality might reflect the non-universality of the conditions that were prevalent when the stars were formed. The obvious suspects are the density of the gas and the condition of ambient background radiation. A key open question is whether this variation in the IMF can be understood theoretically based on first principles.

It is important to emphasize that lensing and dynamical measurements constrain the total normalization of the IMF and not its specific form. Therefore, by themselves they cannot constrain the shape of the IMF and reveal whether the change in the normalization is due to a change in the abundance of low-mass stars or remnants of high-mass stars or any combination thereof. Independent constraints such as those from stellar population diagnostics or from galaxies at different redshifts probing different ranges in stellar mass are necessary to break this degeneracy in the interpretation of the trend.

A final issue that we have not addressed in this paper is how much of the trend shown in Fig. 5 is due to a varying IMF and how much is due to varying dark matter content. For the higher velocity dispersion SLACS galaxies weak and strong lensing and dynamical data allowed Auger et al. (2010b) to disentangle the two effects, showing that the most likely explanation is that both the dark matter content and the normalization of the IMF increase with galaxy mass (see also Cardone et al. 2009; Grillo & Gobat 2010; Tortora et al. 2010, 2011, 2012; Dutton et al. 2011a; Thomas et al. 2011; Deason et al. 2012).

Future papers of this series (Barnabè et al. 2012; Dutton et al., in preparation) will combine the lensing information with dynamical models of kinematic observations to construct two component mass models and disentangle the luminous and dark components for the SWELLS sample as well (see Trott et al. 2010; van de Ven et al. 2010; Suyu et al. 2011; Paper II). This will allow us to differentiate trends in the stellar IMF from trends in dark matter content over the entire range in velocity dispersion.

6 SUMMARY AND CONCLUSIONS

In this paper we have presented complete multiband *HST* imaging (including new images obtained as part of our cycle 18 *HST* programme, GO-12292) for the largest currently known sample of gravitational lens systems where the deflector is an inclined discy galaxy. The SWELLS sample consists to date of 20 secure lenses and six probable lenses.

For each secure lens and one probable lens, we have derived gravitational lens models based on a single isothermal ellipsoid deflector plus external shear. In addition we have used the multicolour *HST* imaging to estimate the stellar mass of the bulge and disc component of each deflector based on SPS models. We have used the two measurements of stellar and total mass within the critical curve to study the normalization of the stellar IMF for spiral lens galaxies.

Our main conclusions can be summarized as follows.

- (i) The ratio between stellar mass and total mass within the critical curve correlates with the velocity dispersion of the deflector galaxy. By combining the SWELLS sample with the SLACS sample of more massive early-type galaxies, we find that the trend extends between 160 and 350 km s⁻¹. This trend can be due to variations in the normalization of the stellar IMF and/or in non-baryonic dark matter content.

(ii) At the low velocity dispersion end (below 230 km s^{-1}) the Salpeter IMF predicts, unphysically, that the mass in stars is greater than the total mass.

(iii) Based on a rigorous probabilistic model, we find that the probability that the true stellar masses are lighter than implied by the Salpeter IMF is 98 per cent for galaxies with velocity dispersion below 230 km s^{-1} , neglecting the contribution of cold gas. If the contribution of cold gas is taken into account, the probability increases to greater than 99 per cent, and a 95 per cent upper limit on the stellar masses is 80 per cent of the mass implied by the Salpeter IMF.

(iv) The light IMF required for low-mass spiral galaxies is at variance with the Salpeter or heavier IMF required for more massive early-type galaxies, consistent with a non-universal stellar IMF.

ACKNOWLEDGMENTS

AAD acknowledges financial support from a CITA National Fellowship, from the National Science Foundation Science and Technology Center CfAO, managed by UC Santa Cruz under cooperative agreement no. AST-9876783. AAD and DCK were partially supported by NSF grant AST 08-08133 and by *HST* grants AR-10664.01-A, HST AR-10965.02-A and HST GO-11206.02-A. PJM was given support by the TABASGO and Kavli foundations, and the Royal Society, in the form of research fellowships. TT acknowledges support from the NSF through CAREER award NSF-0642621, and from the Packard Foundation through a Packard Research Fellowship. LVEK acknowledges the support by an NWO-VIDI programme subsidy (programme number 639.042.505). This research is supported by NASA through *Hubble Space Telescope* programmes GO-10587, GO-10886, GO-10174, 10494, 10798, 11202, 11978 and 12292, and in part by the National Science Foundation under grant no. PHY99-07949 and is based on observations made with the NASA/ESA *Hubble Space Telescope* and obtained at the Space Telescope Science Institute, which is operated by the Association of Universities for Research in Astronomy, Inc., under NASA contract NAS 5-26555, and at the W. M. Keck Observatory, which is operated as a scientific partnership among the California Institute of Technology, the University of California and the National Aeronautics and Space Administration. The Observatory was made possible by the generous financial support of the W. M. Keck Foundation. The authors wish to recognize and acknowledge the very significant cultural role and reverence that the summit of Mauna Kea has always had within the indigenous Hawaiian community. We are most fortunate to have the opportunity to conduct observations from this mountain. Funding for the SDSS and SDSS-II was provided by the Alfred P. Sloan Foundation, the Participating Institutions, the National Science Foundation, the US Department of Energy, the National Aeronautics and Space Administration, the Japanese Monbukagakusho, the Max Planck Society and the Higher Education Funding Council for England. The SDSS was managed by the Astrophysical Research Consortium for the Participating Institutions. The SDSS website is <http://www.sdss.org/>.

REFERENCES

- Auger M. W., Treu T., Bolton A. S., Gavazzi R., Koopmans L. V. E., Marshall P. J., Bundy K., Moustakas L. A., 2009, ApJ, 705, 1099
- Auger M. W., Treu T., Bolton A. S., Gavazzi R., Koopmans L. V. E., Marshall P. J., Moustakas L. A., Burles S., 2010a, ApJ, 724, 511
- Auger M. W., Treu T., Gavazzi R., Bolton A. S., Koopmans L. V. E., Marshall P. J., 2010b, ApJ, 721, L163
- Auger M. W., Treu T., Brewer B. J., Marshall P. J., 2011, MNRAS, 411, L6
- Barnabè M., Czoske O., Koopmans L. V. E., Treu T., Bolton A. S., Gavazzi R., 2009, MNRAS, 399, 21
- Barnabè M., Auger M. W., Treu T., Koopmans L. V. E., Bolton A. S., Czoske O., Gavazzi R., 2010, MNRAS, 406, 2339
- Barnabè M., Czoske O., Koopmans L. V. E., Treu T., Bolton A. S., 2011, MNRAS, 415, 2215
- Barnabè M. et al., 2012, MNRAS, in press (arXiv:1201.1692)
- Bastian N., Covey K. R., Meyer M. R., 2010, ARA&A, 48, 339
- Bell E. F., de Jong R. S., 2001, ApJ, 550, 212
- Bennert V. N., Auger M. W., Treu T., Woo J.-H., Malkan M. A., 2011, ApJ, 726, 59
- Bershady M. A., Verheijen M. A. W., Swaters R. A., Andersen D. R., Westfall K. B., Martinsson T., 2010, ApJ, 716, 198
- Bershady M. A., Martinsson T. P. K., Verheijen M. A. W., Westfall K. B., Andersen D. R., Swaters R. A., 2011, ApJ, 739, L47
- Bolton A. S., Burles S., Koopmans L. V. E., Treu T., Moustakas L. A., 2006, ApJ, 638, 703 (B06)
- Bolton A. S., Burles S., Koopmans L. V. E., Treu T., Gavazzi R., Moustakas L. A., Wayth R., Schlegel D. J., 2008, ApJ, 682, 964 (B08)
- Brewer B. J., Lewis G. F., Belokurov V., Irwin M. J., Bridges T. J., Evans N. W., 2011a, MNRAS, 412, 2521
- Brewer B. J., Pártay L. B., Csányi G., 2011b, Statistics Comput., 21, 649
- Brewer B. J. et al., 2011c, ApJ, 733, L33
- Brownstein J. R. et al., 2012, ApJ, 744, 41
- Cappellari M., 2002, MNRAS, 333, 400
- Cappellari M. et al., 2006, MNRAS, 366, 1126
- Cappellari M. et al., 2012, Nat. preprint (arXiv:1202.3308)
- Cardone V. F., Tortora C., Molinaro R., Salzano V., 2009, A&A, 504, 769
- Chabrier G., 2003, PASP, 115, 763
- Conroy C., Gunn J. E., White M., 2009, ApJ, 699, 486
- de Vaucouleurs G., 1948, Ann. Astrophys., 11, 247
- Deason A. J., Belokurov V., Evans N. W., McCarthy I. G., 2012, ApJ, 748, 2
- Dutton A. A. et al., 2011a, MNRAS, 416, 322
- Dutton A. A. et al., 2011b, MNRAS, 417, 1621 (Paper II)
- Dutton A. A., Mendel J. T., Simard L., 2012, MNRAS, in press
- Ferreras I., Saha P., Leier D., Courbin F., Falco E. E., 2010, MNRAS, 409, L30
- Gallazzi A., Charlot S., Brinchmann J., White S. D. M., 2006, MNRAS, 370, 1106
- Grillo C., Gobat R., 2010, MNRAS, 402, L67
- Hogg D. W., 1999, preprint (astro-ph/9905116)
- Keeton C. R., Kochanek C. S., 1998, ApJ, 495, 157
- Koopmans L. V. E. et al., 2009, ApJ, 703, L51
- Kormann R., Schneider P., Bartelmann M., 1994, A&A, 284, 285
- Kroupa P., 2001, MNRAS, 322, 231
- Kroupa P., Weidner C., Pflamm-Altenburg J., Thies I., Dabringhausen J., Marks M., Maschberger T., 2011, preprint (arXiv:1112.3340)
- Newman A. B., Treu T., Ellis R. S., Sand D. J., 2011, ApJ, 728, L39
- Padmanabhan N. et al., 2004, New Astron., 9, 329
- Panter B., Jimenez R., Heavens A. F., Charlot S., 2007, MNRAS, 378, 1550
- Peng C. Y., Ho L. C., Impey C. D., Rix H.-W., 2002, AJ, 124, 266
- Salpeter E. E., 1955, ApJ, 121, 161
- Sérsic J. L., 1968, Atlas de Galaxias Australes. Observatorio Astronomico, Cordoba, Argentina
- Skilling J., 2006, Bayesian Analysis, 4, 833
- Sonnenfeld A., Treu T., Gavazzi R., Marshall P. J., Auger M. W., Suyu S. H., Koopmans L. V. E., Bolton A. S., 2011, preprint (arXiv:1111.4215)
- Spinelli C., Koopmans L. V. E., Trager S. C., Czoske O., Treu T., 2011, MNRAS, 417, 3000
- Suyu S. H. et al., 2011, ApJ, in press (arXiv:1110.2536)

- Thomas J. et al., 2011, MNRAS, 415, 545
 Tortora C., Napolitano N. R., Romanowsky A. J., Jetzer P., 2010, ApJ, 721, L1
 Tortora C., Napolitano N. R., Romanowsky A. J., Jetzer P., Cardone V. F., Capaccioli M., 2011, MNRAS, 418, 1557
 Tortora C., La Barbera F., Napolitano N. R., de Carvalho R. R., Romanowsky A. J., 2012, MNRAS, submitted
 Treu T., 2010, ARA&A, 48, 87
 Treu T., Auger M. W., Koopmans L. V. E., Gavazzi R., Marshall P. J., Bolton A. S., 2010, ApJ, 709, 1195
 Treu T., Dutton A. A., Auger M. W., Marshall P. J., Bolton A. S., Brewer B. J., Koo D. C., Koopmans L. V. E., 2011, MNRAS, 417, 1601 (Paper I)
 Trott C. M., Treu T., Koopmans L. V. E., Webster R. L., 2010, MNRAS, 401, 1540
 van Albada T. S., Sancisi R., 1986, Philos. Trans. R. Soc. Series A, 320, 447
 van de Ven G., Falcón-Barroso J., McDermid R. M., Cappellari M., Miller B. W., de Zeeuw P. T., 2010, ApJ, 719, 1481
 van Dokkum P. G., Conroy C., 2010, Nat, 468, 940

APPENDIX A: COMPARISON OF LENS MODELS WITH PREVIOUS MODELS

The SWELLS sample contains six spiral lens galaxies that were originally discovered and modelled in SLACS. As a sanity check, we compare the inferred Einstein radii of these lenses from the models presented in this paper with those reported by Auger et al.

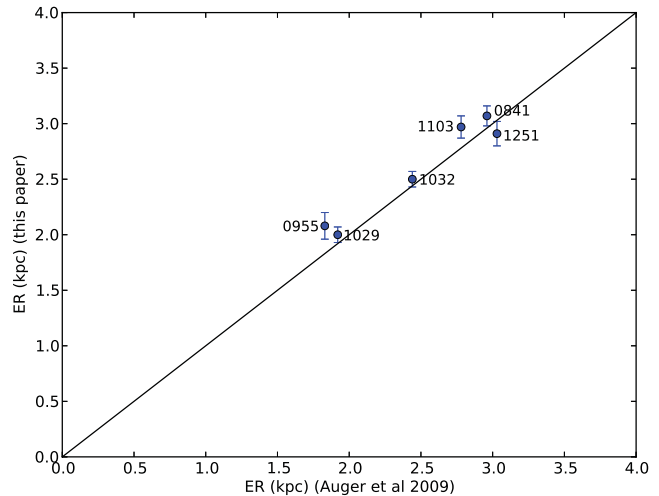


Figure A1. A comparison of the inferred Einstein radii of lenses included in the SWELLS sample and the SLACS sample. Error bars were not reported by Auger et al. (2009). The solid line is the one-to-one relation. The inferred Einstein radii are consistent between the two studies.

(2009). Since Auger et al. (2009) reported Einstein radii in units of kiloparsecs, we convert our Einstein radii to kiloparsecs also. The comparison is shown in Fig. A1 and demonstrates agreement between the two sets of models.

This paper has been typeset from a $\text{\TeX}/\text{\LaTeX}$ file prepared by the author.